ADVANCED MATERIALS INTERFACES
Open Access
www.advmatinterfaces.de

Mechanism of Hydration Induced Stiffening and Subsequent Plasticization of Polyamide Aerogel

*Krisztián Moldován, Attila Forgács, Geo Paul, Leonardo Marchese, Adél Len, Zoltán Dudás, Sándor Kéki, István Fábián, and József Kalmár**

The mesoporous polyamide (PA) aerogel similar in chemical structure to DuPont's Kevlar is an advanced thermal insulation material tested in airspace applications. Unfortunately, the monolithic aerogel readily absorbs humidity (from moist air), which dramatically alters its mechanical properties. The compressive strength of the PA aerogel first increases when its water content increases, but subsequently decreases following additional hydration. To provide a coherent explanation for this non-monotonic change, the aerogel is hydrated stepwise and its hydration mechanism is elucidated by multiscale experimental characterization. The molecular structure is investigated by solid-state and liquid-state nuclear magnetic resonance (NMR) spectroscopy, and the morphology by small angle neutron scattering (SANS) at each equilibrium hydration state. The physico-chemical changes in the molecular level and in the nanoscale architecture are reconstructed. The first water molecules bind into the vacancies of the intermolecular H-bonding network of the PA macromolecules, which strengthens this network and causes concerted morphological changes, leading to the macroscopic stiffening of the monolith. Additional water disrupts the original H-bonding network of the macromolecules, which causes their increased segmental motion, marking the start of the partial dissolution of the nanosized fibers of the aerogel backbone. This eventually plasticizes the monolith.

1. Introduction

The term aerogel is used to describe a family of open porous solids that can be fabricated from a wide variety of base materials, e.g. inorganic oxides, carbon, biopolymers, synthetic polymers.[1] The chemical structure of the backbone and the nanoscale morphology provide advanced and tunable properties for these aerogels, such as low density, high specific surface area, low dielectric constants and low thermal conductivity.[2,3] Due to their unique properties, aerogels are promising functional materials for a diverse range of specialty applications, mainly as advanced thermal management layers, supercapacitors, and electrode materials.[4] The constraint of the wide scale use of aerogels is generally their poor mechanical properties, such as brittleness and poor machinability.[5] This problem has been overcome in the case of the archetypical silica aerogel using chemical cross-linking strategies or preparing composites. Reinforced silica aerogels are manufactured at the industrial scale for advanced thermal management application.[5,6]

Besides reinforced silicas, the most promising aerogels close to reach the technology readiness level needed for commercialization are synthetic polymer aerogels, mainly polyurea, polyimide and polyamide.[7] Pekala was the first who prepared durable polymer aerogels from formaldehyde and resorcinol.[8] During the last decade, many types of synthetic

K. Moldován, A. Forgács, I. Fábián, J. Kalmár
ELKH-DE Mechanisms of Complex Homogeneous and Heterogeneous Chemical Reactions Research Group
Department of Inorganic and Analytical Chemistry
University of Debrecen
Egyetem tér 1., Debrecen H-4032, Hungary
E-mail: kalmar.jozsef@science.unideb.hu

The ORCID identification number(s) for the author(s) of this article can be found under https://doi.org/10.1002/admi.202300109

DOI: 10.1002/admi.202300109

K. Moldován
Doctoral School of Chemistry
University of Debrecen
Egyetem tér 1., Debrecen H-4032, Hungary
G. Paul, L. Marchese
Department of Science and Technological Innovation
Universitá del Piemonte Orientale
Viale T. Michel 11, Alessandria 15121, Italy
A. Len, Z. Dudás
Neutron Spectroscopy Department
Centre for Energy Research
Konkoly-Thege Miklós út 29–33, Budapest H-1121, Hungary
S. Kéki
Department of Applied Chemistry
University of Debrecen
Egyetem tér 1., Debrecen H-4032, Hungary

polymer aerogels were designed with the primary aim of developing superinsulators with good mechanical properties in a wide temperature range.[9–12] Among these materials, polyimide and polyamide aerogels have the most promising properties enabling aerospace and electronic applications.[13–16] In general, the cost of polyimide aerogels are high due to the need of expensive chemicals for synthesizing the polymer backbone.[17] The major advantages of polyamide aerogels are the more reasonable cost, and the straightforward synthesis route, providing advantageous properties, such as high durability and low thermal conductivity similar to those of the polyimide aerogels.[14,18] Polyamide aerogels received attention because of potential space applications as insulation materials for cryogenic tanks, rovers, and habitats.

One of the constraints of the applications of polyimide and polyamide aerogels is the possibility of extensive structural changes upon the sorption of water vapor. Because of this sensitivity, considerable efforts were taken to prepare moisture resistant aerogels by tailoring their chemical structures.[19,20] In spite of the practical importance, there are only a handful of studies reporting the hydration mechanism of synthetic polymer aerogels. Recently the hydration of a polyimide aerogel was investigated using SANS in endpoint measurements by contrasting the dry and the fully hydrated aerogels.[21] The hydration of nanostructured biopolymers and polymers is accompanied by complicated changes both in their molecular structure and in their nanoscale architecture.[22–24] In the case of aerogels, the exact nature of these changes and the mechanism of the hydration of the backbone can be elucidated in fine details only by the combination of state-of-the-art characterization techniques that provide information on the molecular level structural changes, as well as the alteration of the nanoscale architecture.[25–29] Another complication is, that water is known to be a Janus-type small molecular additive in polymer science; capable of both the plasticization and the anti-plasticization of the same polymer in a concentration dependent manner.[30–32]

Nuclear magnetic resonance (NMR) methods have been proven to be powerful tools for exploring the physical interactions of water molecules with the nanostructured backbones of mesoporous materials. This is possible through the exchange of magnetization between water and the pore wall, the alteration of the translational diffusion of water and the alteration of the phase change mechanisms of water due to nanostructuring. These properties of water molecules are measured by liquid-state NMR relaxometry, diffusiometry, and cryoporometry that are complemented by solid-state NMR measurements providing information on the chemical structure and magnetization dynamics of the solid backbone in interaction with water.[33–36]

In this study, a linear polyamide gel similar in chemical structure to Kevlar was synthesized, and a monolithic aerogel was produced from it by drying in supercritical CO_2 using a published recipe.[14] The main goal of the study was to understand the molecular basis of the alteration of the physical properties of the monolithic aerogel as a function of its conditioning in moist air. In order to explain the macroscopic changes, the intimate mechanism of the hydration of the aerogel was investigated using multiple solid state and liquid state nuclear magnetic resonance (NMR) spectroscopy techniques in combination with small angle neutron scattering (SANS) measurements.

2. Experimental Section

2.1. Preparation of Polyamide (PA) Aerogel

2.1.1. Chemicals

N-methylpyrrolidinone (NMP), p-phenylenediamine (pPDA), anhydrous calcium chloride ($CaCl_2$), and terephthaloyl chloride (TPC) were purchased from Sigma-Aldrich. Absolute ethanol was purchased from VWR. All reagents were used without further purification. Doubly-deionized and ultrafiltered water (ELGA PureLab classic system) was used for hydrating the aerogel samples for the structural studies.

2.1.2. Aerogel Preparation

The synthetic procedure was taken from a previous publication and reproduced without any modification.[14] Briefly, $CaCl_2$ (2.25 g, 20.3 mmol) and pPDA (3.45 g, 31.9 mmol) were dissolved in NMP (90.0 mL) and cooled to 0 °C. Upon cooling, an opaque suspension formed. Solid TPC (6.32 g, 31.1 mmol) was added, which resulted in the dissolution of the particles and the formation of a transparent yellow solution. After 5 min of stirring, the solution became cloudy and the viscosity increased due to the formation of polyamide in the reaction of pPDA and TPC (**Scheme 1**). The thick suspension was poured into Teflon molds and aged for 16 h at room temperature. The resulting cylindrical gel monoliths were removed from the molds and soaked in anhydrous ethanol for 5 days with the solvent being removed and replaced with fresh ethanol each day. Once this solvent exchange process was complete, the gels were dried using supercritical CO_2. The drying apparatus and the process were described in detail in a previous publication.[37] The as-prepared polyamide aerogel was denoted PAA through the paper.

2.2. Controlled Hydration of PA Aerogel

The as-prepared PAA was defined as the dry aerogel. Partially hydrated aerogel samples were prepared by increasing the water content of PAA in a controlled and stepwise manner up to adding 3.0 mg water to 1.0 mg PAA. The dry aerogel was gently broken to small pieces, placed onto an analytical balance (min. 50 mg PAA) and aliquots of water were added. Water content was defined as grams of liquid water added to grams of dry aerogel (g/g). The partially hydrated samples were gently mixed and sonicated for 10 min using a bath type sonicator. It was tested that sonication does not cause any structural change in the hydrated samples. Each sample was prepared in the corresponding sample holder (NMR tubes or quartz cuvettes), and sealed airtight for a 24 h equilibration period before the measurements. The measurements were reproduced in duplicates in such way that the same water content was set by two different methods in duplicate samples; either by directly hydrating the dry aerogel, or by adding

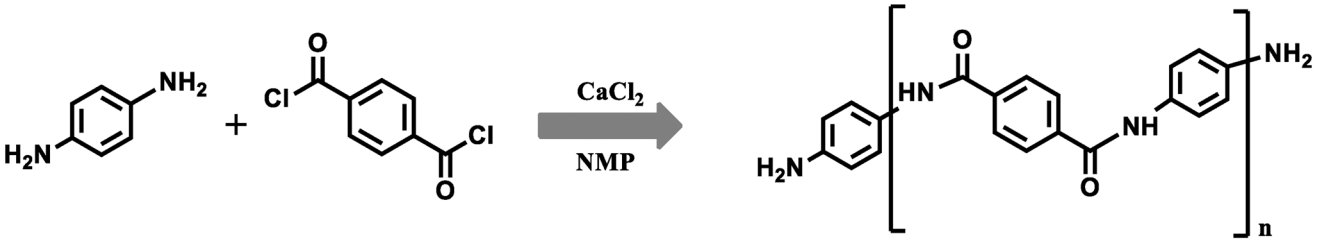

Scheme 1. The formation and the chemical structure of the linear polyamide (PA) macromolecules.

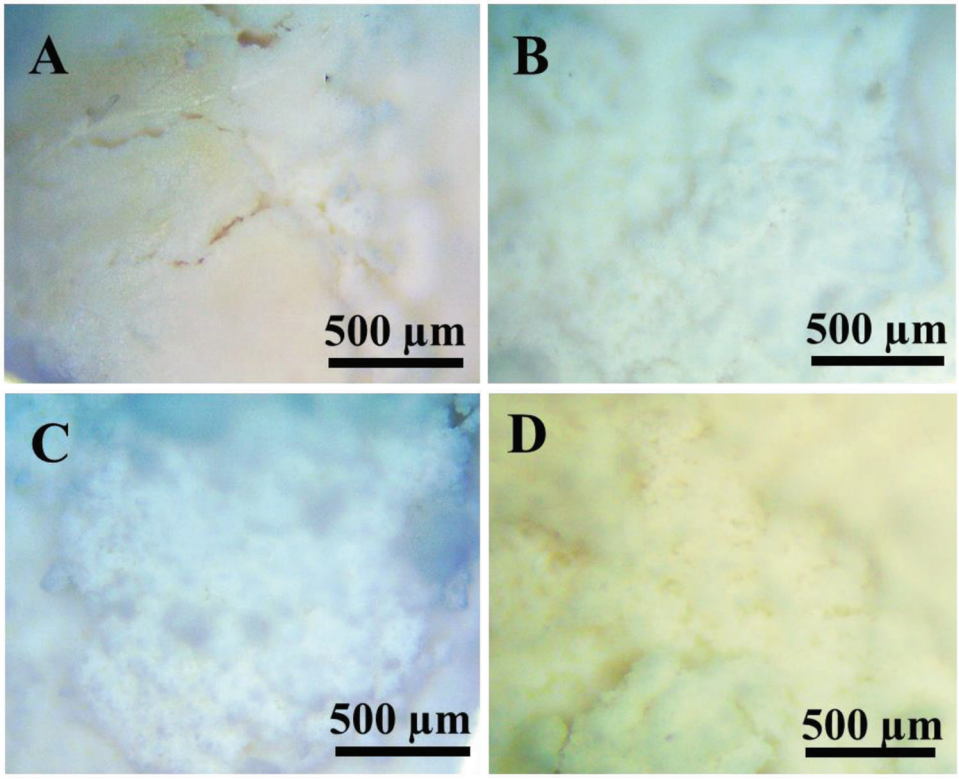

Figure 1. Light microscopy images of monolithic polyamide aerogel (PAA) pieces. Dry, as-prepared aerogel A); and hydrated PAA of 0.19 B), 0.37 C) and 2.2 D) g/g water content.

additional aliquots of water to samples of lower water contents. The results of such duplicate experiments were identical within the reproducibility of the experiments. Light microscopy images of dry and hydrated monolithic PAA pieces are shown in **Figure 1**.

Another procedure to prepare partially hydrated aerogel samples was the equilibration of PAA monoliths with humid air for 84 h in sealed desiccators. The humidity of the air was controlled by placing saturated solutions of appropriate inorganic salts into the desiccators.[38] (The composition of the solutions is given in Table S1, Supporting Information.) The water contents of the hydrated aerogel samples were calculated from the weight loss of the samples after drying at 90 °C. The final water content of the aerogel was proportional to the relative humidity of the air. Equilibration at 50% and 100% relative humidity yields hydrated aerogel samples of 0.16 ± 0.01 and 0.36 ± 0.01 g/g water content, respectively.

2.3. Characterization of Dry and Hydrated Aerogel Samples

2.3.1. Conventional Characterization Techniques

The morphology of the as-prepared PAA was studied by low-voltage scanning electron microscopy (LV-SEM) in a ThermoFisher Scientific Scios 2 instrument. The samples were fixed on vacuum-resistant carbon tapes. The electron beam resolution was 1.6 nm at the optimum working distance (<5 mm) at 2 kV accelerating voltage. Because of the low accelerating voltage and the small electron beam current, the charging effects of the aerogel were negligible.[39] Therefore, sputter coating was not applied. Extra care was taken to image freshly fractured surfaces far from the point of splitting of the monolithic aerogel.

Nitrogen adsorption–desorption porosimetry measurements were performed with a Quantachrome Nova 2200e Surface Area

and Porosity Analyzer (Quantachrome Instruments, USA). The sample was outgassed in a vacuum at 40 °C for 24 h before the measurements. Data were evaluated with the NovaWin 11.0 software. The apparent surface area was calculated using the multipoint BET method based on 5 points in the adsorption isotherm until $p/p_0 = 0.30$.[40] Pore size distribution was calculated from the desorption isotherm using the Barret-Joyner-Halenda (BJH) model assuming cylindrical pore geometry in the calculation.

The chemical identity of PAA was confirmed by attenuated total reflection Fourier transform infrared spectroscopy (ATR-FTIR) measured in a Perkin Elmer Spectrum Two Spectrometer in the frequency range from 4000 to 450 cm^{-1}.

2.3.2. Compression Tests

The compressive strength of dry and partially hydrated PAA monoliths was measured using an Instron 4302 Universal Strength Testing Apparatus (Instron, Darmstadt, Germany). The crosshead speed of the probe was 1.0 mm min^{-1}. A standard strength testing head of 1.0 kN was used. Monolithic test objects of regular cylindrical shape were used with the length of 28 ± 3 mm and the diameter of 20 ± 2 mm. Extra care was taken to use monoliths with parallel top and bottom sides. The aerogel monoliths were measured either in their as-prepared states, or after pre-conditioning in controlled humidity air. Each measurement was replicated using at least 3 individual monoliths synthesized in different batches and conditioned independently. The specimen-to-specimen relative standard deviation of the measured data was ca. 15%.

Data collection was controlled by the INSTRON Series IX Automated Materials Tester v.8.30.00 software. The experimental data was evaluated using two approaches. First, the Young's modulus was calculated using the classical considerations by the instrument controlling software. Second, the full strain-stress curves were fitted using the extended version of the standard linear solid (SLS) viscoelastic model, as detailed later.

2.3.3. Small Angle Neutron Scattering (SANS)

Dry, powdered PAA was loaded into 2 mm thick quartz cuvettes and measured without any pre-treatment. Partially hydrated PAA samples were prepared in the same quartz cuvettes by directly adding D_2O. The measurements were performed at the Budapest Neutron Centre in the Yellow Submarine pin-hole type instrument using a 2D neutron detector.[41] The Beaucage model was applied for data fitting in the whole experimental Q range using the SasView 5.0.3 open source software.[42–44] The experimental and theoretical details are given in the Supporting Information and in previous publications.[28,45]

2.3.4. Solid-State NMR Spectroscopy

Solid state NMR spectra were acquired on a Bruker Avance III 500 spectrometer and a wide bore 11.75 Tesla magnet with operational frequencies for ^1H and ^{13}C of 500.13 and 125.77 MHz, respectively. In order to optimize the sensitivity of the probe, the rotor was fitted with Teflon inserts to define a 50 ml volume.[46] The partially hydrated PAA samples were prepared directly in the 4 mm ZrO_2 rotor. The details are given in the Supporting Information.

2.3.5. NMR Relaxometry

The NMR relaxometry measurements were performed in a Minispec Bruker mq20 relaxometer. The dry PAA was titrated with water.[34,47,48] The water / dry aerogel mass ratio was increased to 0.6 g/g in 11 steps, and subsequently to 3.0 g/g in additional 12 steps. The multiple T_2 values of the different relaxation domains of water were combined in the final signal, because the exchange of the water molecules was slow between the domains.[49,50] Inverse Laplace transformation was used to identify the individual exponential functions in the primary CPMG decays as detailed in the Supporting Information and in previous publications.[28,51]

2.3.6. NMR Cryoporometry

Partially hydrated PAA samples were characterized by NMR cryoporometry at different water contents in a Bruker Avance II 360 MHz NMR instrument. The Carr-Purcell-Meiboom-Gill (CPMG) spin-echo pulse sequence was applied to eliminate the ^1H signal of the solid phase. The experiments were optimized using hydrated mesoporous silica aerogel as a reference material.[52] Temperature was calibrated using glycol and methanol.[53] The relaxation filtered signal intensity of hydrated PAA changed gradually with the temperature, as water froze or ice melted. The melting and freezing mechanisms of liquids in confined spaces show a hysteresis in general.[35,54,55] The size distribution of the confined water droplets was calculated using the methodology of Petrov and Furó.[35] The experimental and theoretical details are given in the Supporting Information and in previous publications.[27,28]

2.3.7. NMR Diffusiometry

The self-diffusion of water was studied in partially hydrated PAA at different water contents at 298 K. A stimulated echo pulse sequence (PGSTE) was used for the measurements featuring bipolar gradients and longitudinal eddy current delay (BIPLED).[33,56,57] The spectra were transformed with MestReNova 9.0 software and evaluated according to the classical considerations.[58,59] The different diffusion domains were separated using inverse Laplace transformation as detailed previously.[60–62] The experimental and theoretical details are given in the Supporting Information.

2.4. Data Analysis (Statistical Analysis)

The methodology of data pre-processing and data presentation, the sample sizes, the calculation and statistical methods and the softwares used for data analysis are given for each method in the dedicated subsections above and in the Supporting Information.

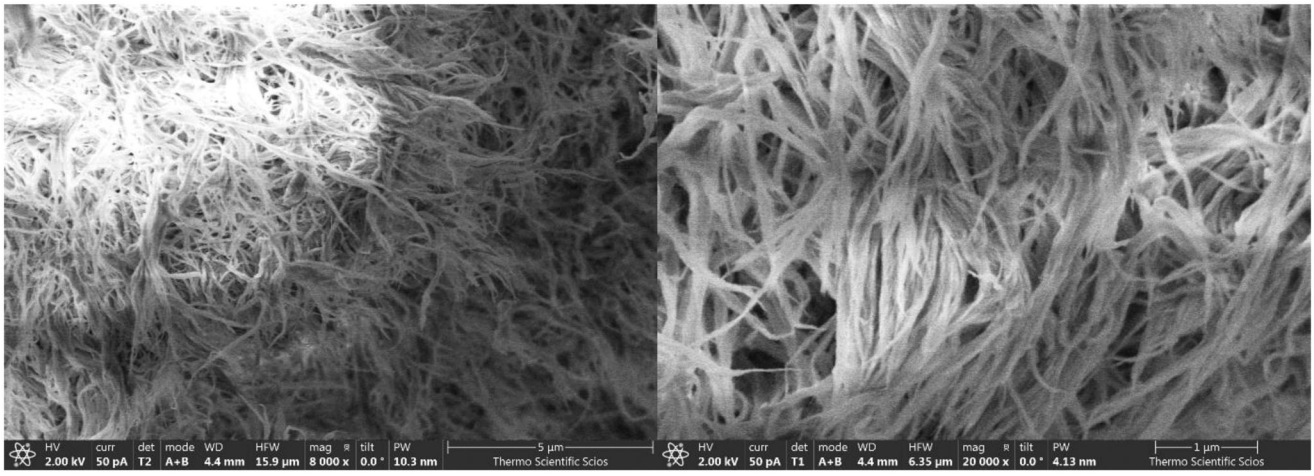

Figure 2. Representative LV-SEM images of the pristine polyamide aerogel (PAA).

3. Results and Discussion

The structure of this section is as follows. First, the characterization of the pristine PAA is presented. This is followed by showing that the hydration of the monolithic PAA causes dramatic changes in its mechanical properties in a non-monotonic way. Finally, the hydration mechanism of PAA is elucidated to provide an explanation for this phenomenon.

3.1. Scanning Electron Microscopy (SEM)

Representative LV-SEM images of pristine PAA are shown in **Figure 2**. The main structural elements dominating the morphology are strut-like polymer fibrils. The 3D skeletal architecture of PAA (i.e., the aerogel backbone) consists of these entangled and interconnected fibrils.[14] The thickness and the length of the primary fibrils vary to a large extent. Some of the fibrils are branched and some struts merge by the ends. The PA macromolecules forming the fibrils are held together by secondary chemical bonds, as discussed later. The interaction between the individual fibrils is physical entanglement. There are structural regions where the fibrils are positioned in partially ordered parallel lines, but the majority of the fibrils are randomly oriented and tortuous. The structural regions in the aerogel backbone where fibrils entangle or merge are termed "focal points".

In the present fibrillar architecture "pores" are best defined as the void spaces among the loosely interweaved fibrils. There are no geometrical elements or solid boundaries that clearly separate these void spaces from each other. Thus, there are no such well-defined pores in PAA as in inorganic (e.g., silica) aerogels or in biopolymer (e.g., Ca-alginate) aerogels. As a consequence, the interconnectivity of the pore system of PAA, as well as, the variation of the size and the shape of the voids are very high. Thus, the interpretation of the characterization data has to be meticulous, because the classical geometrical models generally used for the calculations have limited validity in this case.

3.2. N_2-Sorption Porosimetry

The representative N_2 adsorption-desorption isotherms of PAA are shown in **Figure 3**A. The isotherms fit into the IUPAC IV category including the H3 type hysteresis loop. The shape of the isotherms and the well-pronounced hysteresis is characteristic for mesoporous materials. The steep increase at the lowest relative pressures indicates the presence of micropores. Macropores that cannot completely be filled with condensed N_2 are also present in PAA, as seen in the SEM images. The structural parameters calculated by the classical BET and BJH evaluation methods are collected in **Table 1**, and the pore size distribution is given in Figure 3B.

The morphology of PAA (cf. Figure 2) should carefully be taken into account when assessing the calculated structural parameters, because the N_2-sorption method is not sensitive to open pores larger than 150 nm. Therefore, the extensive macroporosity of PAA does not significantly contribute to the calculated mesopore volume, and it is only partially represented in the pore size distribution curve. This is one of the limitations of the N_2-sorption method extensively discussed in the literature.[63] The envelope density of PAA is 0.23 g cm^{-3}, while the density of its polymer skeleton is 1.27 g cm^{-3}.[14] The large difference between the calculated total pore volume (3.5 cm^{-3} g) and the measured mesopore volume (0.7 cm^{-3} g) reflects the extensive macroporosity of PAA.

The BJH pore size distribution of PAA is apparently bimodal (Figure 3B). However, the narrow peak around $d_{pore} \approx 4$ nm, which is the result of the deviation between the adsorption and the desorption isotherms at low relative pressures might not be real, because this deviation can be due to the partial dissolution of the PA fibers by liquid N_2 causing the alteration of the aerogel structure and the isotherms. The mesopores with a wide size distribution starting at $d_{pore} \approx 15$ nm are characteristic for this family of fibrillar aerogels. The more sophisticated NL-DFT method could not be used for data evaluation here, because of the lack of an appropriate kernel.

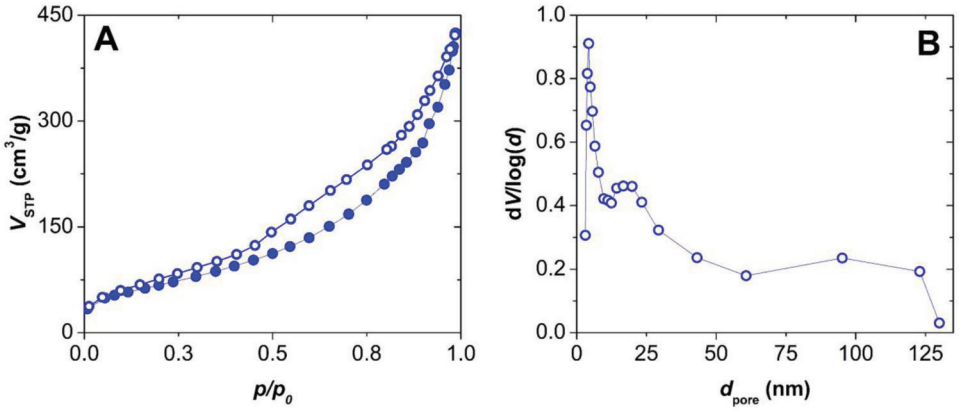

Figure 3. Panel A: Nitrogen adsorption-desorption isotherms of PAA. Panel B: Pore size distribution calculated from the desorption isotherm using the BJH method.

Table 1. Structural parameters of pristine PAA estimated by the BET and the BJH methods from the N_2 adsorption-desorption data (Figure 3).

Parameter	PAA	Data evaluation
***C*-constant**	59 ± 3	BET
Specific surface area (m^2 g^{-1})	251 ± 20	BET
Total mesopore volume (cm^3 g^{-1})	0.7 ± 0.1	BJH

3.3. IR Spectroscopy

The positions and relative intensities of the characteristic peaks in the FT-IR spectrum of the pristine PAA (Figure S1, Supporting Information) are in excellent agreement with the literature data, which confirms the chemical identity of the aerogel.[14] Accordingly, the IR spectrum is in excellent agreement with the ssNMR data, as discussed later. The major IR peaks of PAA correspond to polyamides as assigned in the Supporting Information.[64]

3.4. Compression Tests

The experimental strain-stress curves and the values of the Young's modulus are shown in **Figure 4**. The full experimental strain-stress curves were mathematically fitted using the extended version of the standard linear solid (SLS) viscoelastic model, which was developed for describing the bulk phase mechanical features of novel polyurethane and epoxy-polyurethane polymers. The detailed theoretical considerations and the steps of data evaluation are given in a previous publication.[65] The estimated values of the strain energy at break for the dry and partially hydrated PAA monoliths are given in Figure 4 as a function of conditioning.

Starting from the dry aerogel, the Young's modulus and the compressive strength of the monolithic PAA dramatically increase when its water content increases, and display maxima following conditioning in 50% relative humidity, i.e., at ca. 0.16 g/g water content. Interestingly, the additional hydration of PAA causes a sharp decrease in these mechanical parameters.

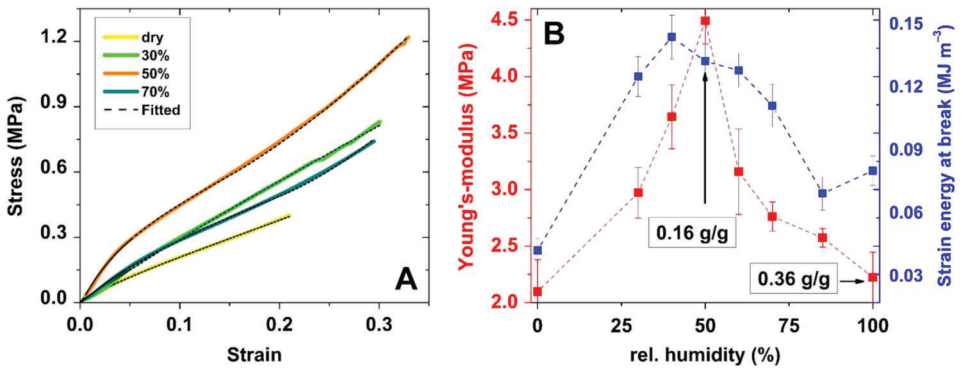

Figure 4. Results of monolithic PAA compression tests. Panel A: Representative strain-stress curves of the dry and the partially hydrated aerogel monoliths. The relative humidity used for conditioning the monoliths is given in the legend. The black curves are results of mathematical fitting by the standard linear solid (SLS) viscoelastic model. Panel B: The estimated Young's modulus and compressive strength of the monolithic PAA as a function of its conditioning in humid air. The measured water contents are given in the legend. The error bars represent the specimen-to-specimen standard deviation of the experimental data.

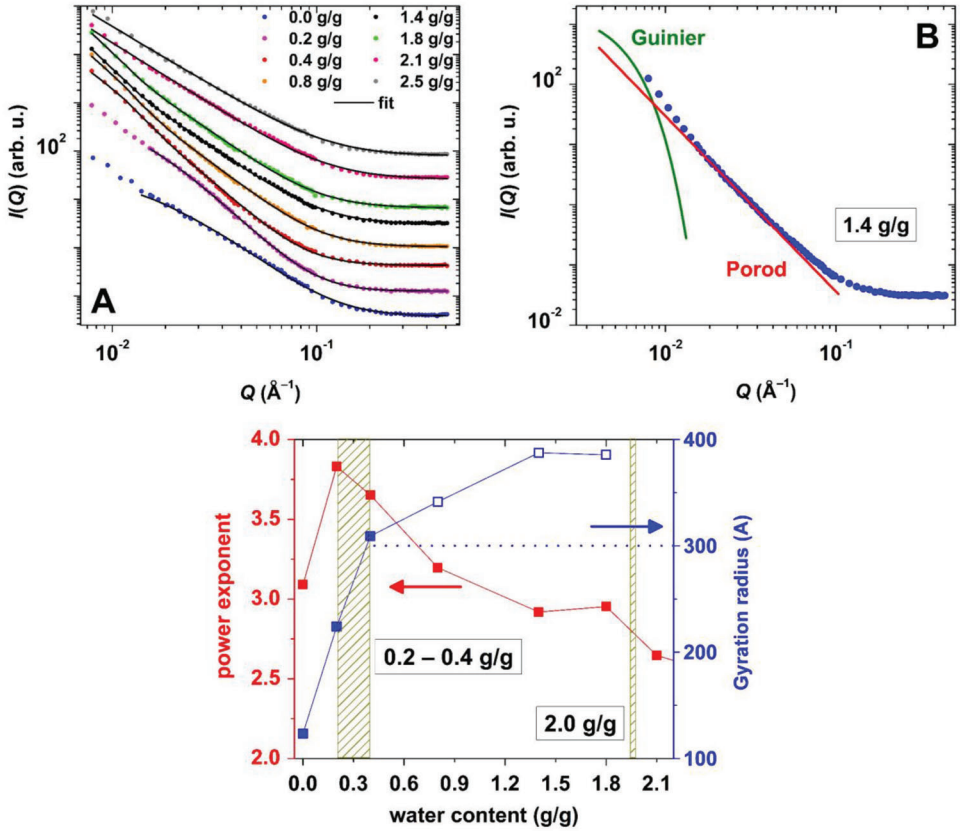

Figure 5. Small angle neutron scattering (SANS) characterization of partially hydrated PAA. Panel A: The experimental SANS curves (markers) together with the best fits (lines), as given in the Supporting Information. The water contents of the PAA samples are given in the legend. Panel B: Contribution of the different model functions to the overall fit. Panel C: Estimated structural parameters as a function of the water content of PAA. (The deviation between duplicate measurements is ca. 10%.) The estimated R_g values are uncertain above 300 Å. The dashed vertical bars indicate water contents of special interest.

In order to give an explanation for this phenomenon, the hydration mechanism of the PA aerogel was studied on multiple scales. The molecular level processes were probed by various NMR methods, and the alterations in the nanostructure were investigated by SANS.

3.5. Small Angle Neutron Scattering (SANS)

The experimental scattering curves are shown in **Figure 5**A together with the best fits. The Beaucage model is adequate for fitting the curves until 0.4 g/g water content. Above this water content, the Guinier regions of the SANS curves gradually shift toward the small Q values out of the experimental range, as shown in Figure 5B. Therefore, the R_g values obtained from the Beaucage model fits can only be treated as estimated values, assuming similar structural elements in the aerogel as at low water contents, but with increased average pore sizes. The SANS curves are less structured at water contents higher than 1.8 g/g, and can be fitted only with the simple power-law model (Porod region). The estimated structural parameters are shown as a function of the water content in Figure 5C. Several mathematical models were tested for fitting the scattering curves, but only the present approach was found consistent for describing the whole range of the investigated samples.[63,66]

The R_g steeply increases with increasing water content up to ca. 0.4 g/g. At higher water contents, the increase of the R_g is approximately gradual. The p exponent has a maximum value at ca. 0.2 g/g water content ($p \approx 4$), and decreases from this point on in a gradual manner with increasing water content until $p < 3$. The process of parameter estimation and the interpretation of the gyration radius (R_g) is further discussed in the Supporting Information.

The SANS results demonstrate the dramatic change of the nanoscale morphology of the PA aerogel as a function of its water content.[63,66] The increase of R_g is associated with the increase of the size of the pores, which is naturally accompanied by the initial smoothening of the surface of the pore walls as shown by the $p \approx 4$ value at 0.2 g/g water. Above this water content, the size of the pores still increases, although, the roughness of the pore walls also increase. The p value is between 3 and 4 in this region of hydration, which indicates surface fractal-like structures and points out that the smooth surface becomes rough again as a consequence of additional hydration. The explanation is the partial dissolution of the fibers of the aerogel backbone as a consequence of the significant conformational changes and the increased segmental motion of the PA macromolecules.[22,67] Evidence for the

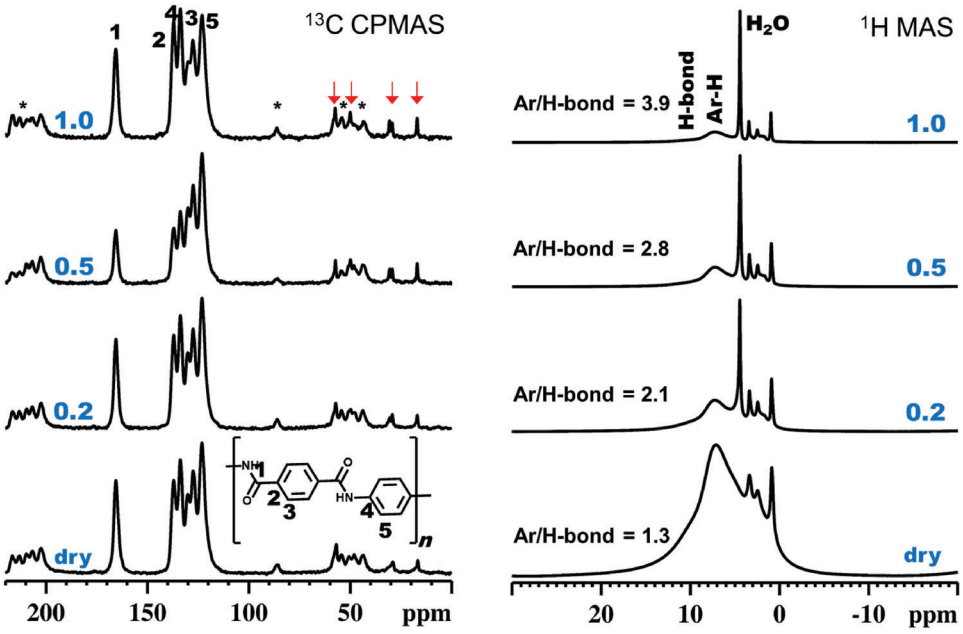

Figure 6. The mass-loading normalized ^{13}C CPMAS (left panel) and ^{1}H MAS (right panel) NMR spectra of the PAA samples of different water contents, as shown in the panels in g/g units. The chemical formula of PA and the assignment of the peaks are given in the panels. The explanation of the spectral changes as a function of the water content is given in the main text. The ^{13}C CPMAS spectra were recorded using a MAS rate of 10 kHz and a CP contact time of 0.5 ms. The MAS rate was 15 kHz for the ^{1}H MAS. Spectra are normalized to the highest peak intensity. The peaks of residual solvents are marked by red arrows and the spinning sidebands by asterisks.

molecular level changes of the aerogel structure is supported by the solid-state and the liquid-state NMR results, as discussed in the next sections. At water contents higher than 2.0 g/g, the *p* exponent is lower than 3 indicating the formation of a mass fractal-like structure in the hydrated aerogel. This is attributed to the formation of well-defined nano-sized water droplets in the focal points of the hydrated aerogel backbone, which is strongly supported by the NMR relaxometry and cryoporometry results, as discussed in the next sections. The rationale is, that these small individual water droplets cannot be detected by SANS, however, the mass fractal scattering behavior of the extensively hydrated PA network indicates their existence. (A systematic overview on the effect of the gradual addition of D_2O regarding the SANS contrast is given in the Supporting Information.)

The formation of a hydrogel at high water contents can be ruled out due to the absence of sharp changes in the *p* exponent. This is in contrast to the features of biopolymer aerogels.[28] According to the SANS data, marked structural changes take place in the PA aerogel when reaching the critical water content of ca. 0.2 g/g, and subsequently when reaching 2.0 g/g. The nature of these marked structural changes is further elucidated in the next sections based on the compiled results of the various independent NMR techniques.

3.6. Solid-State NMR

The mass-loading normalized ^{13}C CPMAS and ^{1}H MAS NMR spectra of the dry and the partially hydrated PAA samples are shown in **Figure 6**. The assignment of the peaks was performed based on literature data.[14] The ^{13}C CPMAS spectrum of the dry PAA is in excellent agreement with the published data and confirms its expected chemical structure (Scheme 1). Consequently, the ssNMR data are in good accordance with the FT-IR spectrum of the PAA.

The high resolution of the ^{13}C CPMAS peaks of PAA allowed the unambiguous assignation of the five aromatic resonances. The NMR line widths of the pristine PAA dried in supercritical CO_2 are comparable with those reported for bulk Kevlar materials.[68,69] This means that the 3D organization of the PA macromolecules in the fibrous aerogel backbone is similar to those in bulk Kevlar materials. The high intensity shoulder at ca. 10 ppm in the ^{1}H MAS spectrum of the dry PAA is indicative of the presence of multiple intermolecular H-bonds among the polymer molecules, which is characteristic for the linear polyamides.

Hydrating PAA does not alter the ^{13}C chemical shifts, or the peak widths and resolution, yet cause marked changes in the relative peak intensities, which becomes expressed at ≈0.5 g/g water content. This indicates the significant reorientation of the polymer chains at higher water contents. The accompanying marked decrease in the ^{13}C CPMAS intensities is attributed to the increased segmental motion of the polymer chains when reaching this critical hydration level, which lowers the effectiveness of the magnetic cross-polarization.[22,67]

In-line with this, the ^{1}H MAS spectra of the partially hydrated samples show that the extensive intermolecular H-bonding network of the linear PA molecules is gradually disrupted with the increasing hydration of the aerogel.[70] The ratio of the aromatic protons to the ones participating in strong inter-molecular H-bonds between the PA molecules was derived from the quantitative ^{1}H MAS NMR (Ar/H-bond values in Figure 6) by curve

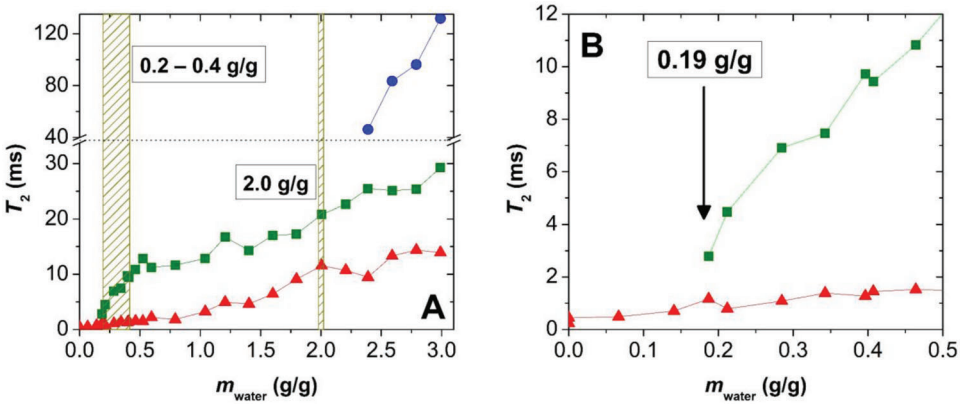

Figure 7. Results of the NMR-relaxometry study of partially hydrated PAA. Both panels show the values of the longitudinal relaxation times (T_2) as the function of the water content of PAA. Panel B is a magnification of Panel A; the data points are the same on the two panels. (The deviation between duplicate measurements is ca. 10%.) Three relaxation domains (marked with red triangles, green squares, and blue circles) were observed at the different hydration levels until the saturation of pores of the aerogel by water at ca. 3.0 g/g. The dashed vertical bars indicate water contents of special interest.

fitting. This value is 1.3 for the dry aerogel; and it increases to 3.9 at 1.0 g/g water content indicating a significant decrease in the number of intermolecular H-bonds in the partially hydrated PA network.[71]

Proton chemical shifts are sensitive to structural changes, however, it is possible that the aromatic moieties participate in non-covalent interactions, such as π-stacking. These effects cannot be identified based on the ^{13}C and ^{1}H MAS NMR data. The molecular level structural changes taking place in the PAA as a result of its gradual hydration was further elucidated by compiling the results of the ssNMR and the liquid phase NMR relaxometry measurements. This is discussed in the next section.

3.7. NMR Relaxometry

The longitudinal (spin-spin) relaxation times (T_2) of water protons can be distinct depending on the chemical environment of the corresponding water molecules. Therefore, the water molecules localized in the different regions of a nanostructured material and participating in different chemical interactions with the solid backbone can be classified and characterized based on their respective T_2 values.[47,72]

Naturally, water molecules bound by strong secondary chemical bonds (e.g., H-bonds) to the PA molecules in the primary hydration sphere of the aerogel backbone have characteristically low T_2. Water molecules in the secondary hydration sphere or the ones forming puddles or droplets in the focal points of the PAA backbone have significantly higher relaxation times. Protons in these different chemical environments are in exchange with one another, mainly because of the re-localization of the water molecules. Because the exchange is relatively slow on the timescale of the NMR relaxometry experiments (ca. 1 ms), multiple relaxation domains are observed corresponding to the different chemical environments.[28,73] Finally, the variation of the characteristic parameters of the relaxation domains as a function of the water content of the aerogel gives information on the hydration mechanism of the solid backbone and the filling of the nanostructured porous system by water.[47–49,51]

The PAA was gradually hydrated, and the T_2 relaxation times of water were recorded as a function of water content. This represents the equilibrium sates of the partially hydrated PAA samples. The saturation of the pores by water is reached at a water content of ca. 3.0 g/g. The compiled results of the NMR relaxometry measurements are shown in **Figure 7**. (The raw data is shown in the Supporting Information together with the best fits and the demonstration of the use of the inverse Laplace transformation for identifying the number of domains.)

At the lowest water contents, there is only one relaxation domain detectable with very small T_2 values. This domain corresponds to water molecules in strong interaction, mainly in H-bonding with the PA macromolecules.[70] The 2nd domain appears at ca. 0.19 g/g water content with significantly bigger T_2 values. However, these T_2 values are not high enough to indicate the formation of well-defined water droplets in the pores at this hydration level. Accordingly, the 2nd domain corresponds to water molecules still in strong interaction with the PA backbone. The amplitudes associated with the decay signals of the first two domains are in correlation with each other even at small water contents indicating the exchange of water between these domains. Based on the similarity of the amplitude values, the amount of water associated with the two domains is approximately at low water contents.

The difference in the chemical environments of the water molecules of the 1st and the 2nd domains can be elucidated based on the ssNMR results (cf. Section 3.6). The first water molecules form H-bonds with the PA macromolecules on the surface of the fibers and build into the existing network of H-bonds (**Scheme 2**) that is corroborated by previous studies.[74–77]

This binding mode does not cause dramatic changes in the ^{13}C CPMAS spectrum. When the vacant H-bonding sites are saturated at ca. 0.19 g/g water content, the additional water molecules enter into the fibers, insert in-between the PA macromolecules and disrupt their intermolecular H-bonding network present in the dry aerogel (Scheme 2).[77–78] This becomes expressed in the ^{13}C CPMAS spectrum at ca. 0.5 g/g water content. The segmental motion of the PA macromolecules increases, and their original orientations are altered in parallel to the formation and evolution

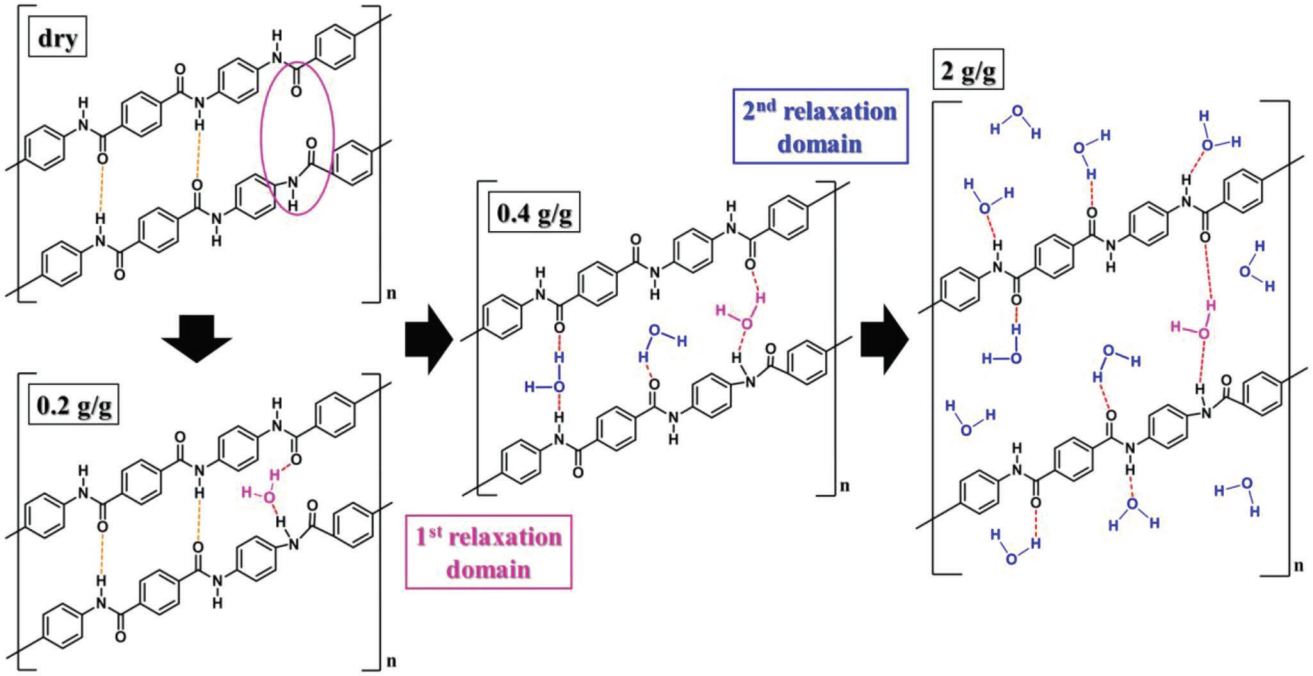

Scheme 2. Schematic representation of the interaction of water with the PA macromolecules as a function of the water content of the aerogel (displayed in the legend). The first portion of water molecules (1st relaxation domain) occupy the empty H-binding sites in the intermolecular H-bonding network of the linear PA macromolecules. The additional hydration results in the insertion of water molecules (2nd relaxation domain) between polymer chains, which eventually results in the partial dissolution of the PA fibers at high water contents.

of the 2nd relaxation domain. This process is the starting point of the hydration of the bulk of the fibers, or in another terminology, the beginning of the partial dissolution of the fibers. When water molecules insert in-between the PA macromolecules, their conformation significantly change, which alters the morphology of the aerogel backbone. The associated morphological changes are well-expressed in the alteration of the SANS curves measured until ca. 0.4 g/g water (cf. Section 3.5).

This mechanistic theory for the hydration of PAA is in good agreement with the observed sharp decrease of the compressive strength of the partially hydrated aerogel starting above ca. 0.16 g/g water content (cf. Section 3.4), which is concerted with the appearance of the 2nd NMR relaxation domain and the dramatic change of the SANS curves.[77–78]

The additional increase of the water content above 0.5 g/g results in the extensive hydration and partial dissolution of the bulk of the PA fibers. Water molecules are in less and less constraint in the well-hydrated fibers, therefore, the T_2 values of the first two relaxation domains increase. Evidently, water molecules in the different regions of the PA backbone exchange with one another. Finally, a third relaxation domain appears at ca. 2.0 g/g water. The T_2 values of the 3rd domain are significantly bigger than those of the first two domains, which corresponds to the formation of well-defined water droplets and puddles in the focal points of the entangled fibers of the aerogel backbone. The sharp increase of the T_2 values of the 3rd domain indicate the dramatic increase of the size of the puddles until the saturation of the porous system by water at ca. 3.0 g/g.

An important observation is that the appearance of the 3rd domain at high water contents does not alter the gradual increase of the T_2 values of the 2nd domain. Because the T_2 values of the 2nd domain are characteristic for water built into hydrated polymer fibers, this finding suggests the conservation of the fibrous structure of the aerogel even when it is saturated with water. This argument is further strengthened by the absence of a sharp decrease of the SANS power exponent at high water contents, which would be indicative for the transformation of the backbone into a hydrogel with fully solvated single polymer chains, rather than distinct fibers. Despite the significant morphological changes, the PA aerogel backbone remains well-defined even when flooded by water, and the material does not form a hydrogel. For comparison, hydrogel formation is characteristic for biopolymer aerogels, which causes dramatic, yet concerted changes in the NMR relaxometry and the SANS data.[28]

3.8. NMR Diffusiometry

Two variables were changed in the NMR diffusiometry measurements: i) the water content of the PA aerogel, and ii) the observation time of the experiments.[52] Such approach yields information on the hydration mechanism and the permeability of the PA network via the alteration of the self-diffusion coefficient of water due to its confinement in the nanostructured aerogel.[21,25] The observed self-diffusion coefficient (D_{obs}) depends on the hydration level and the morphology of the porous system. The latter can be probed by changing the observation time of the diffusion experiment. The effective displacement of the water molecules in the tortuous network is a function of the observation time, and thus, affects D_{obs}. The behavior of water

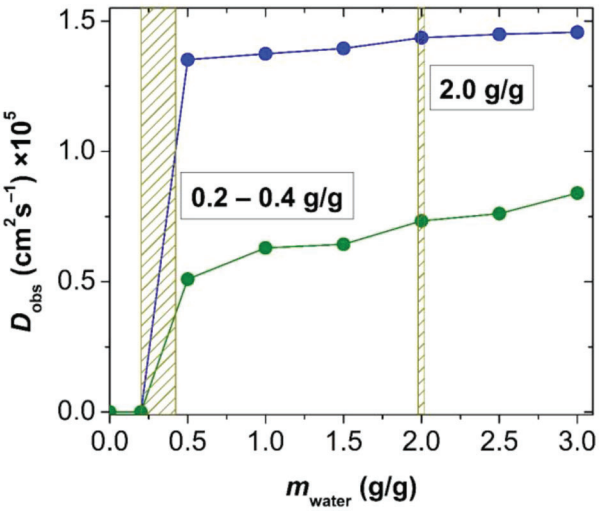

Figure 8. The observed self-diffusion coefficients (D_{obs}) of water as a function of the water content of the partially hydrated PAA. (The deviation between duplicate measurements is ca. 10%.) The self-diffusion of water is not detectable below 0.5 g/g water content. Two diffusion domains are present at higher water contents. For comparison, $D = 2.30 \times 10^{-5}$ cm^2 s^{-1} in the pure phase of bulk water.[79] The dashed vertical bars indicate water contents of special interest.

molecules forming the various diffusion domains can be distinct at different hydration levels depending on their localization and chemical environment in the aerogel.[60,62]

The measured D_{obs} values are shown in **Figure 8** as a function of the water content of PAA. The self-diffusion of water is not detectable below ca. 0.5 g/g water content. At higher water contents, two diffusion domains were identified based on the inverse Laplace transformation and the non-linear fitting of the raw data, as described in details in the Supporting Information. The two domains were identified with acceptable statistical reliability in each sample independently of the hydration level. The D_{obs} values of both domains increase gradually with the increasing water content of PAA, but only to a slight extent. The D_{obs} values are invariant of the observation time of the NMR experiment at every studied hydration level.

The diffusion domains can be assigned based on the numerical values of D_{obs}, and taking into account the structural data collected by the other techniques. The dislocation of the water molecules bound to the PA macromolecules by strong H-bonds in the 1st NMR relaxation domain is very limited.[70,80] Furthermore, the T_2 values of these water protons are very small, and thus, the PGSTE sequence acts as a relaxation filter for these protons.[28] Consequently, no water diffusion is observed in the hydrated aerogel until the saturation of these primary binding sites at ca. 0.2 g/g of water content. By increasing the hydration level, the appearance of the diffusion signal is coincident with the sharp increase of the signal of the 2nd relaxation domain (cf. Figure 7). The first diffusion domain ($D_{obs} \approx 0.6 \times 10^{-5}$ cm^2 s^{-1}) represents the water molecules diffusing inside the hydrated PA fibers, which is naturally hindered.[80,81] In comparison, water molecules forming a surface layer on the hydrated PA fibers or forming droplets and puddles are more mobile, and yield a second, faster diffusion domain ($D_{obs} \approx 1.4 \times 10^{-5}$ cm^2 s^{-1}). The two diffusion domains are mathematically separable, however, water molecules exchange between these domains on the timescale of the diffusion experiments.[82]

The time scale of the diffusion experiments (ca. 100 ms) is significantly longer than that of the relaxation experiments (ca. 1 ms). During this time, water molecules inside the fibers can exchange with those in the mobile regions, which results in the detection of a second, faster diffusion domain. Consequently, the second diffusion domain appears at a lower water content than the 3rd relaxation domain associated with well-defined droplets and puddles of water in the aerogel pores. The explanation is that at low hydration levels, only a very low proportion of the water molecules is localized on the surface of the fibers or in droplets, which is undetectable by relaxometry. The amount of such water reaches the level of detection at water contents above 2.0 g/g in relaxometry.

The slight increase of the D_{obs} values of the domains with the increasing water content of the aerogel is due to the increased amount and mobility of water in the partially dissolved fibers, and due to the increase of the size of water droplets and puddles in the pores.

The D_{obs} values of both domains are independent of the observation time of the diffusion experiment, suggesting that the structural regions where the water molecules translocate are continuous at least in the low micrometer scale. This is evidence for the preservation of the highly interconnected fibrillar structure of the aerogel even at high water contents.

3.9. NMR Cryoporometry

The primary data in the NMR cryoporometry measurements are the relaxation filtered intensities of the liquid water protons as a function of temperature. The relaxation delay in the applied CPMG sequence is long enough to achieve the complete transversal relaxation of the water molecules in the frozen phase and those in strong association with the solid aerogel backbone.[26,55,83] Due to this effect, the partially hydrated PA aerogel displays a meaningful ^{1}H NMR signal only at water contents higher than 1.0 g/g. Representative melting-freezing curves are shown in **Figure 9** for samples of different hydration.

The principle in this measurements is the detection of the shift of the phase transition temperatures of water confined in various geometries in the nanoscale by the fibrous network of the aerogel backbone.[35,36] The sizes and the shapes of the water bodies confined in the aerogel, referred to as droplets and puddles were reconstructed based on the measured shifts of the melting and freezing temperatures, as detailed in the Supporting Information.

The relaxation filter of the CPMG sequence was optimized to remove the signal of the protons in frozen water, but this necessarily filters out the fast-relaxing 1st and 2nd domains in the partially hydrated PAA that are associated with water molecules strongly bound to the aerogel backbone (cf. Section 3.7). Therefore, the low intensity hysteresis loop detected in the cryoporometry curves at 1.0 g/g water content suggest that minor but mobile "freezing" water bodies are present in the system even before the detection of the 3rd relaxation domain.[84] Thus, the NMR cryoporometry and diffusiometry

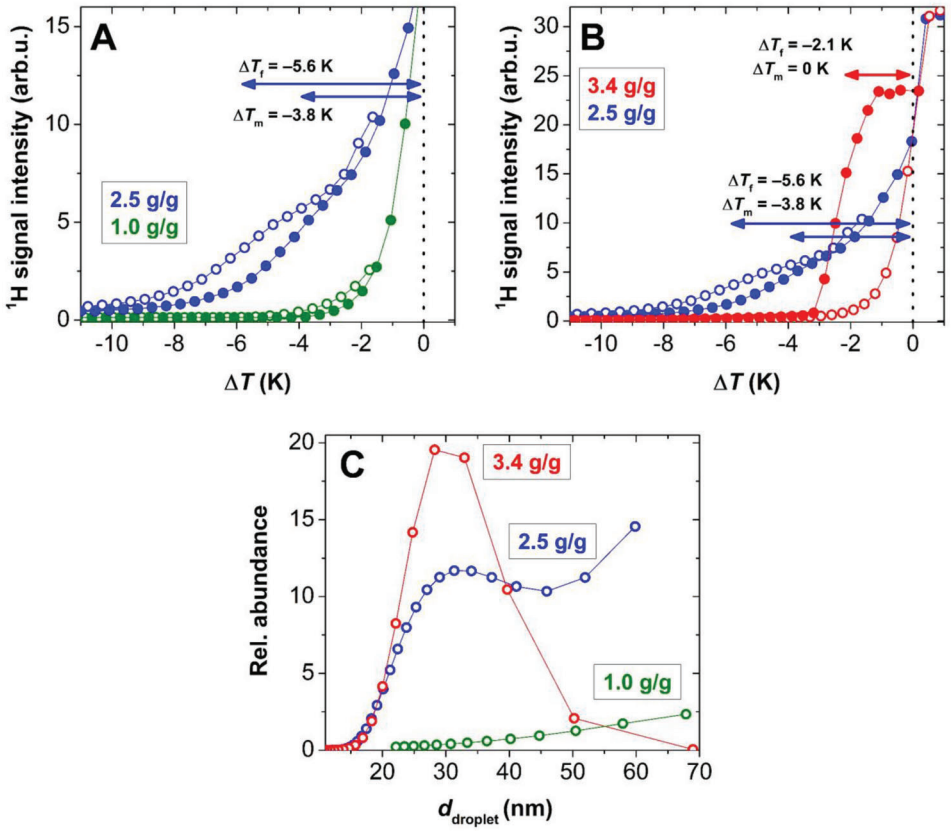

Figure 9. NMR cryoporometry data of hydrated PAA samples. The water content of PAA is given in the legend. Panels A and B: Normalized melting-freezing curves measured at different water contents. The arrows indicate the temperature depressions in the hysteresis curves. The $\Delta T_f/\Delta T_m$ ratio is ca. 3:2 at 2.5 g/g water content, indicating dominantly spherical droplet shape. The $\Delta T_m = 0$ K at 3.4 g/g water content, indicating slab shaped water puddles. Panel C: Size distribution of the water droplets and puddles reconstructed from the freezing curves. (The deviation between duplicate samples is less than 15%.) The values at 1.0 g/g are strongly biased by relaxation effects.

results support each other, since the existence of such mobile water accounts for the presence of the faster diffusion domain even at low water contents (cf. Figure 8). Owing to the relaxation transfer arising from the intermediate exchange between the domains, the CPMG signal is regarded quantitative only at water contents higher than 2.0 g/g, which is the start of the formation of well-defined droplets giving rise to the 3rd relaxation domain.

At 2.5 g/g water content, the shape of the well-defined melting-freezing hysteresis loop follows the approximate $\Delta T_f/\Delta T_m$ ratio of 3:2. This indicates that the majority of the confined water bodies are spherical. The corresponding droplet sizes calculated using Equations S6 and S7 (Supporting Information) are significantly larger than the original mesopore sizes of the dry aerogel (cf. Figure 3). This is in agreement with the significant increase of the SANS gyration radius following the hydration of PAA (cf. Figure 5). The complimentary results of these techniques are strong indication suggesting that the pore sizes of PAA dramatically increase due to its hydration. The forming ice crystals might deform the fibrous backbone, but this would be indicated by the distortion of the melting-freezing hysteresis loop in the subsequent cycles, which is not the case here.

The cryoporometry measurements conducted at 3.4 g/g water content indicate that the confined water bodies in the hydrated aerogel take the geometry of extensive slabs, because there is no detectable melting point depression ($\Delta T_m = 0$ K) accompanying the decrease of the freezing point, as seen in Figure 9B. Polymer fibrils passing through larger bodies of water change the geometry of confinement, leading to the change of the shape of the hysteresis loop. The width of the slabs in this case is representative for the width of the continuous water bodies, which is in good agreement with the previously measured size of the water droplets at 2.5 g/g water content (Figure 9C). This is further evidence for the conservation of the well-defined backbone of the PA aerogel exerting confinement even at its complete hydration.

The cryoporometry results show that the void spaces (pores) of the hydrated PAA are only partially filled with water bodies at 2.5 g/g water content. These water bodies are separated and confined among the hydrated PA fibrils at first, but merge and fill the available slit-like void spaces at 3.4 g/g water content without significantly changing the backbone architecture.

3.10. Hydration Mechanism

Based on the compiled results of ssNMR, liquid state NMR and SANS, the major steps of the hydration of the PAA are summarized graphically in **Scheme 3**. The molecular events and the alteration of the nanoscale architecture are concerted. These

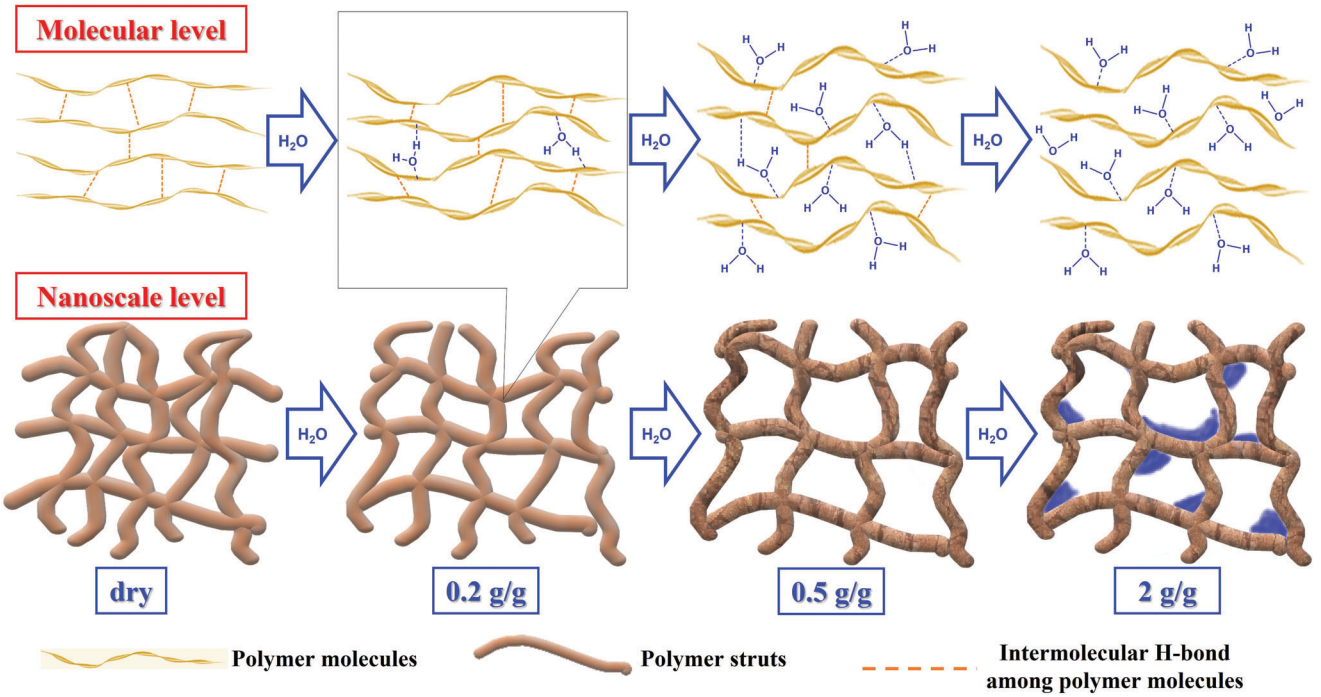

Scheme 3. Graphical representation of the different stages of the hydration of the PA aerogel. The concerted molecular level events and nanoscale rearrangements are depicted in respective panels. The detailed description of the hydration mechanism is given in the text.

multi-scale structural changes are definite in governing the macroscopic properties of the aerogel, and account for even such a complicated phenomenon as the non-monotonic change of the compressive strength of the monolithic aerogel as a function of its hydration level.

The first water molecules bind to the surface of the PA fibers (struts) and fill the vacancies in the intermolecular H-bonding network of the PA macromolecules.[74–76] Water molecules bound in the fibers in this manner are associated with the first 1st NMR relaxation domain, regarded to be structural water and practically immobile. These water molecules strengthen the H-bonding network stabilizing the fibers, which causes the rearrangement of the nanostructure of the aerogel,[85] as detected by SANS. The strengthening of the fibers and their rearrangement are together responsible for the increasing stiffness of the monolithic aerogel. As indicated by several techniques, the primary sites are saturated at ca. 0.2 g/g water content of PAA, and the additional hydration causes dramatic structural changes.

In this stage, between ca. 0.2 g/g and 0.4 g/g, water molecules enter into the bulk of the PA fibers, insert in-between the macromolecules and occupy some of their H-bonding sites. This disrupts the intermolecular H-bonding network characteristic for the dry aerogel. As a consequence, the conformation of the macromolecules rearranges and their segmental motion increases. This causes the macroscopic plasticization of the monolithic aerogel.[30–31,78] The insertion of water molecules and the disruption of the original H-bonding network is complete at ca. 0.4 g/g water content.

Additional hydration causes the partial dissolution of the fibers, which further increases the pore sizes. This is accompanied by the increasing surface roughness of the partially dissolved PA fibers. The combined results of NMR diffusiometry and cryoporometry suggest that a small portion of water forms a minor mobile layer on the surface of the fibers above ca. 0.5 g/g water. Nevertheless, most of the water is absorbed in the hydrated PA fibers at this stage, which causes their further dissolution and the increased mobility of water inside. Well-defined water droplets and puddles form only above ca. 2.0 g/g water content that merge at ca. 3.0 g/g to extensive slabs fully saturating the pores.

The experimental data are consistent in showing that the well-defined fibrous structure of the aerogel is preserved even above 3.0 g/g of water, and no hydrogel formation takes place. This is different form the behavior of most of the biopolymer aerogels, since they tend to form hydrogels when flooded by water.

4. Conclusion

The mesoporous polyamide aerogel (PAA) with the chemical structure of Kevlar absorbs humidity from moist air, which dramatically alters the mechanical properties of the monolith. The changes are non-monotonic; both the Young's modulus and the compressive strength first increase with the increasing water content of the aerogel, and subsequently decrease under extensive hydration. The unique hydration mechanism of PAA accounts for this phenomenon. The initial stiffening of the aerogel is due to the binding of the first portion of water molecules into the vacancies of the intermolecular H-bonding network of the PA macromolecules, which strengthens this network and causes secondary morphological changes in the aerogel backbone. The subsequent water molecules partially dissolve the PA fibers of the backbone by disrupting the original H-bonding network of

the PA macromolecules, which naturally plasticizes the well-hydrated aerogel. The presented results highlight the importance of understanding the hydration of advanced functional materials as one of a key factors altering their performance; furthermore, offer the foundation of gaining control over these features.

Supporting Information

Supporting Information is available from the Wiley Online Library or from the author.

Acknowledgements

The authors greatly acknowledge the anonymous Reviewers' comments for improving the manuscript. The research had been financially supported by the National Research, Development and Innovation Office, Hungarian Science Foundation (OTKA: FK_17-124571) and Thematic Excellence Program (TKP2020-NKA-04) of the Ministry for Innovation and Technology in Hungary. J.K. is grateful for the János Bolyai Research Scholarship of the Hungarian Academy of Sciences. J.K. and K.M. are supported by the New National Excellence Program (ÚNKP-21-5 Bolyai+; ÚNKP-22-3-II-DE-220) of the Ministry for Culture and Innovation from the source of the National Research, Development and Innovation Fund. A.L. is grateful for the Civil Engineering Department of the University of Pécs for financial support.

Conflict of Interest

The authors declare no conflict of interest.

Data Availability Statement

The data that support the findings of this study are available from the corresponding author upon reasonable request.

Keywords

aerogel, hydration, mechanism, NMR, polyamide, SANS

Received: February 7, 2023
Revised: March 28, 2023
Published online:

[1] C. A. García-González, T. Budtova, L. Durães, C. Erkey, P. Del Gaudio, P. Gurikov, M. Koebel, F. Liebner, M. Neagu, I. Smirnova, *Molecules* **2019**, *24*, 1815.
[2] S. S. Kistler, A. G. Caldwell, *Ind Eng Chem* **1934**, *26*, 658.
[3] A. C. Pierre, G. M. Pajonk, *Chem. Rev.* **2002**, *102*, 4243.
[4] I. Smirnova, P. Gurikov, *Annu. Rev. Chem. Biomol. Eng.* **2017**, *8*, 307.
[5] J. P. Randall, M. A. Meador, S. C. Jana, *ACS Appl. Mater. Interfaces* **2011**, *3*, 613.
[6] H. Maleki, L. Durães, A. Portugal, *J. Non-Cryst. Solids* **2014**, *385*, 55.
[7] N. Leventis, *Polymers* **2022**, *14*, 969.
[8] R. W. Pekala, *J. Mater. Sci.* **1989**, *24*, 3221.
[9] N. Leventis, C. Chidambareswarapattar, D. P. Mohite, Z. J. Larimore, H. B. Lu, C. Sotiriou-Leventis, *J. Mater. Chem.* **2011**, *21*, 11981.
[10] M. A. Meador, E. J. Malow, R. Silva, S. Wright, D. Quade, S. L. Vivod, H. Guo, J. Guo, M. Cakmak, *ACS Appl. Mater. Interfaces* **2012**, *4*, 536.
[11] Y. Deng, Y. Pan, Z. Zhang, Y. Fu, L. Gong, C. M. Liu, J. Yang, H. Zhang, X. Cheng, *Adv. Funct. Mater.* **2022**, *32*, 2106176.
[12] Y. Pan, J. Zheng, Y. Xu, X. Chen, M. Yan, J. Li, X. Zhao, Y. Feng, Y. Ma, M. Ding, R. Wang, J. He, *J. Colloid Interface Sci.* **2022**, *628*, 829.
[13] J. C. Williams, M. A. Meador, L. McCorkle, C. Mueller, N. Wilmoth, *Chem. Mater.* **2014**, *26*, 4163.
[14] J. C. Williams, B. N. Nguyen, L. McCorkle, D. Scheiman, J. S. Griffin, S. A. Steiner, M. A. Meador, *ACS Appl. Mater. Interfaces* **2017**, *9*, 1801.
[15] S. L. Vivod, M. A. B. Meador, C. Pugh, M. Wilkosz, K. Calomino, L. McCorkle, *ACS Appl. Mater. Interfaces* **2020**, *12*, 8622.
[16] M. Li, F. Gan, J. Dong, Y. Fang, X. Zhao, Q. Zhang, *ACS Appl. Mater. Interfaces* **2021**, *13*, 10416.
[17] M. A. Meador, C. R. Aleman, K. Hanson, N. Ramirez, S. L. Vivod, N. Wilmoth, L. McCorkle, *ACS Appl. Mater. Interfaces* **2015**, *7*, 1240.
[18] J. Lyu, Z. Z. Sheng, Y. Y. Xu, C. M. Liu, X. T. Zhang, *Adv. Funct. Mater.* **2022**, *32*, 2200137.
[19] M. A. B. Meador, M. Agnello, L. McCorkle, S. L. Vivod, N. Wilmoth, *ACS Appl. Mater. Interfaces* **2016**, *8*, 29073.
[20] H. Guo, M. A. Meador, L. McCorkle, D. J. Quade, J. Guo, B. Hamilton, M. Cakmak, *ACS Appl. Mater. Interfaces* **2012**, *4*, 5422.
[21] S. J. Rinehart, B. N. Nguyen, R. P. Viggiano, M. A. B. Meador, M. D. Dadmun, *ACS Appl. Mater. Interfaces* **2020**, *12*, 30457.
[22] M. J. Ariza, J. Benavente, E. Rodriguez-Castellon, L. Palacio, *J. Colloid Interface Sci.* **2002**, *247*, 149.
[23] N. Hu, L. Lin, E. Metwalli, L. Bießmann, M. Philipp, V. Hildebrand, A. Laschewsky, C. M. Papadakis, R. Cubitt, Q. Zhong, P. Müller-Buschbaum, *Adv. Mater. Interfaces* **2022**, *10*, 2201913.
[24] P. Bettotti, C. A. Maestri, R. Guider, I. Mancini, E. Nativ-Roth, Y. Golan, M. Scarpa, *Adv. Mater. Interfaces* **2016**, *3*, 1500415.
[25] P. M. Kekkonen, A. Ylisassi, V. V. Telkki, *J. Phys. Chem. C* **2014**, *118*, 2146.
[26] Y. Kharbanda, M. Urbanczyk, O. Laitinen, K. Kling, S. Pallaspuro, S. Komulainen, H. Liimatainen, V. V. Telkki, *J. Phys. Chem. C* **2019**, *123*, 30986.
[27] M. Kéri, A. Forgács, V. Papp, I. Bányai, P. Veres, A. Len, Z. Dudás, I. Fábián, J. Kalmár, *Acta Biomater.* **2020**, *105*, 131.
[28] A. Forgacs, V. Papp, G. Paul, L. Marchese, A. Len, Z. Dudas, I. Fabian, P. Gurikov, J. Kalmar, *ACS Appl. Mater. Interfaces* **2021**, *13*, 2997.
[29] R. Digaitis, P. Falkman, V. Oltner, L. E. Briggner, V. Kocherbitov, *Carbohydr. Polym.* **2022**, *291*, 119542.
[30] Y. P. Chang, P. B. Cheah, C. C. Seow, *J. Food Sci.* **2000**, *65*, 445.
[31] L. Mascia, Y. Kouparitsas, D. Nocita, X. Bao, *Polymers* **2020**, *12*, 769.
[32] J. S. Vrentas, J. L. Duda, H. C. Ling, *Macromolecules* **1988**, *21*, 1470.
[33] C. S. Johnson, Jr, *Prog. Nucl. Magn. Reson. Spectrosc.* **1999**, *34*, 203.
[34] P. J. Barrie, *Annu. Rep. NMR Spectrosc.* **2000**, *41*, 265.
[35] O. V. Petrov, I. Furo, *Prog. Nucl. Magn. Reson. Spectrosc.* **2009**, *54*, 97.
[36] J. B. Webber, *Prog. Nucl. Magn. Reson. Spectrosc.* **2010**, *56*, 78.
[37] I. Lazar, I. Fabian, *Gels* **2016**, *2*, 26.
[38] L. B. Rockland, *Anal. Chem.* **1960**, *32*, 1375.
[39] L. Juhasz, K. Moldovan, P. Gurikov, F. Liebner, I. Fabian, J. Kalmar, C. Cserhati, *Polymers* **2021**, *13*, 588.
[40] M. Thommes, K. Kaneko, A. V. Neimark, J. P. Olivier, F. Rodriguez-Reinoso, J. Rouquerol, K. S. W. Sing, *Pure Appl. Chem.* **2015**, *87*, 1051.
[41] L. Almásy, *J. Surf. Invest.: X-Ray, Synchrotron Neutron Tech.* **2021**, *15*, 527.
[42] S. M. King, *Modern techniques for polymer characterisation: Small Angle Neutron Scattering*, (Eds: R. A. Pethrick, J. V. Dawkins), John Wiley & Sons Ltd, Chichester **1999**.
[43] G. Beaucage, *J. Appl. Crystallogr.* **1995**, *28*, 717.
[44] B. Hammouda, *J. Appl. Crystallogr.* **2010**, *43*, 1474.
[45] I. Lázár, A. Forgács, A. Horváth, G. Király, G. Nagy, A. Len, Z. Dudás, V. Papp, Z. Balogh, K. Moldován, L. Juhász, C. Cserháti, Z. Szántó, I. Fábián, J. Kalmár, *Appl. Surf. Sci.* **2020**, *531*, 147232.

[46] G. Paul, C. Bisio, I. Braschi, M. Cossi, G. Gatti, E. Gianotti, L. Marchese, *Chem. Soc. Rev.* **2018**, *47*, 5684.
[47] S. G. Allen, P. C. L. Stephenson, J. H. Strange, *J. Chem. Phys.* **1997**, *106*, 7802.
[48] M. Simina, R. Nechifor, I. Ardelean, *Magn. Reson. Chem.* **2011**, *49*, 314.
[49] I. Bardenhagen, W. Dreher, D. Fenske, A. Wittstock, M. Bäumer, *Carbon* **2014**, *68*, 542.
[50] T. Asakura, K. Isobe, S. Kametani, O. T. Ukpebor, M. C. Silverstein, G. S. Boutis, *Acta Biomater.* **2017**, *50*, 322.
[51] M. Kéri, D. Nyul, K. László, L. Novák, I. Bányai, *Carbon* **2022**, *189*, 57.
[52] J. Kalmar, M. Keri, Z. Erdei, I. Banyai, I. Lazar, G. Lente, I. Fabian, *RSC Adv.* **2015**, *5*, 107237.
[53] C. Ammann, P. Meier, A. Merbach, *J. Magn. Reson.* **1982**, *46*, 319.
[54] J. C. Dore, J. B. W. Webber, J. H. Strange, *Colloids Surf., A* **2004**, *241*, 191.
[55] V. M. Gun'ko, V. V. Turov, R. Leboda, V. I. Zarko, J. Skubiszewska-Zieba, B. Charmas, *Appl. Surf. Sci.* **2007**, *253*, 5640.
[56] Y. Cohen, L. Avram, L. Frish, *Angew. Chem., Int. Ed.* **2005**, *44*, 520.
[57] D. H. Wu, A. D. Chen, C. S. Johnson, *J. Magn. Reson., Ser. A* **1995**, *115*, 260.
[58] M. Kéri, Z. Nagy, L. Novák, E. Szarvas, L. P. Balogh, I. Bányai, *Phys. Chem. Chem. Phys.* **2017**, *19*, 11540.
[59] M. Kéri, C. Peng, X. Shi, I. Bányai, *J. Phys. Chem. B* **2015**, *119*, 3312.
[60] R. Valiullin, V. Skirda, *J. Chem. Phys.* **2001**, *114*, 452.
[61] C. H. Cho, Y. S. Hong, K. Kang, V. I. Volkov, V. Skirda, C. Y. Lee, C. H. Lee, *Magn. Reson. Imaging* **2003**, *21*, 1009.
[62] T. J. Rottreau, C. M. A. Parlett, A. F. Lee, R. Evans, *J. Phys. Chem. C* **2017**, *121*, 16250.
[63] G. Reichenauer, in *Aerogels Handbook*, (Eds: M. A. Aegerter, N. Leventis, M. M. Koebel), Springer, New York **2011**, p. 449.
[64] J. Bandekar, *Biochim. Biophys. Acta* **1992**, *1120*, 123.
[65] L. Nagy, M. Nagy, B. Vadkerti, L. Daroczi, G. Deak, M. Zsuga, S. Keki, *Polymers* **2019**, *11*, 825.
[66] A. Emmerling, J. Fricke, *J. Non-Cryst. Solids* **1992**, *145*, 113.
[67] S. Goudeau, M. Charlot, F. Muller-Plathe, *J. Phys. Chem. B* **2004**, *108*, 18779.
[68] A. D. English, *J. Polym. Sci., B: Polym. Phys.* **1986**, *24*, 805.
[69] J. O. Brauckmann, P. Zolfaghari, R. Verhoef, E. A. Klop, G. A. de Wijs, A. P. M. Kentgens, *Macromolecules* **2016**, *49*, 5548.
[70] H. Kitano, K. Ichikawa, M. Fukuda, A. Mochizuki, M. Tanaka, *J. Colloid Interface Sci.* **2001**, *242*, 133.
[71] G. Paul, S. Steuernagel, H. Koller, *Chem. Commun.* **2007**, *48*, 5194.
[72] B. Maillet, R. Sidi-Boulenouar, P. Coussot, *Langmuir* **2022**, *38*, 15009.
[73] F. Gallego-Gómez, C. Cadar, C. López, I. Ardelean, *J. Phys. Chem. C* **2019**, *123*, 30486.
[74] M. Fukuda, M. Ochi, M. Miyagawa, H. Kawai, *Text. Res. J.* **1991**, *61*, 668.
[75] N. Chaupart, G. Serpe, *J. Near Infrared Spectrosc.* **1998**, *6*, 307.
[76] R. Iwamoto, H. Murase, *J. Polym. Sci., Part B: Polym. Phys.* **2003**, *41*, 1722.
[77] N. S. Murthy, M. Stamm, J. P. Sibilia, S. Krimm, *Macromolecules* **1989**, *22*, 1261.
[78] Y. S. Hu, S. Mehta, D. A. Schiraldi, A. Hiltner, E. Baer, *J. Polym. Sci., Part B: Polym. Phys.* **2005**, *43*, 1365.
[79] M. Holz, S. R. Heil, A. Sacco, *Phys. Chem. Chem. Phys.* **2000**, *2*, 4740.
[80] R. J. Pace, A. Datyner, *Polym. Eng. Sci.* **1980**, *20*, 51.
[81] M. Laurati, P. Sotta, D. R. Long, L. A. Fillot, A. Arbe, A. Alegria, J. P. Embs, T. Unruh, G. J. Schneider, J. Colmenero, *Macromolecules* **2012**, *45*, 1676.
[82] S. Hwang, J. Haase, E. Miersemann, J. Kärger, *Adv. Mater. Interfaces* **2020**, *8*, 2000749.
[83] T. J. Rottreau, G. E. Parkes, M. Schirru, J. L. Harries, M. G. Mesa, P. D. Topham, R. Evans, *Colloids Surf., A* **2019**, *575*, 256.
[84] T. Maeda, K. Yamamoto, T. Aoyagi, *J. Colloid Interface Sci.* **2006**, *302*, 467.
[85] S. Bjorklund, V. Kocherbitov, *J. Colloid Interface Sci.* **2019**, *545*, 289.